Mimicking graphene physics with a plane hexagonal wire mesh

Yulia N. Dautova, Andrey V. Shytov, Ian R. Hooper, J. Roy Sambles, and Alastair P. Hibbins

Citation: Appl. Phys. Lett. **112**, 191601 (2018); doi: 10.1063/1.5026355
View online: https://doi.org/10.1063/1.5026355
View Table of Contents: http://aip.scitation.org/toc/apl/112/19
Published by the American Institute of Physics

Mimicking graphene physics with a plane hexagonal wire mesh

Yulia N. Dautova,[a] Andrey V. Shytov, Ian R. Hooper, J. Roy Sambles, and Alastair P. Hibbins
Department of Physics and Astronomy, University of Exeter, Exeter, Devon EX4 4QL, United Kingdom

(Received 19 February 2018; accepted 16 March 2018; published online 7 May 2018)

A hexagonal metallic-wire mesh is fabricated and experimentally characterized to demonstrate graphene-physics in an electromagnetic analogue. In contrast to previous studies, our structure has a smaller ratio of out-of-plane to in-plane dimensions, more akin to real graphene. This allows for the development of a simple analytical treatment using equivalent electric circuit theory, and we demonstrate that the predicted dispersion curves of the supported eigenmodes agree well with those obtained from experimental measurements. *Published by AIP Publishing.*
https://doi.org/10.1063/1.5026355

Many concepts from solid state physics may be applied to electromagnetic waves propagating in periodic media.[1,2] Since the pioneering works of Yablonovitch and John in 1987,[3,4] artificial metallic and dielectric structures that to some extent mimic natural materials have been created and extensively studied in 1D, 2D, and 3D. Reflecting the analogy with solid state crystals, such structures were named photonic crystals, sometimes also being referred to as electromagnetic crystals. Early photonic crystals were realised at microwave frequencies,[3,4] and this regime remains a good spectral domain for studying physical phenomena that would be more difficult to implement at higher frequencies.

In the last decade, interest in the photonics of artificial graphene, which mimics some aspects of the electronic behaviour of real graphene,[5] has emerged.[6] Because it offers the advantage of having a much higher degree of freedom than real graphene, such an analogue can be used to study phenomena that are difficult or impossible to otherwise explore. For instance, artificial graphene systems allow for the control of the coupling between neighbouring elements and thus manipulation of the band structure.[7,8] By changing the inter-element coupling strength, one gains control over the dispersion gradient at the Dirac crossings, i.e., group velocity. Pseudo-magnetic fields, another intrinsic phenomenon of graphene, is an effect that is rather difficult to observe as it requires the creation of non-trivial patterns of high strain, e.g., "nanobubbles."[9] Such "nanobubbles" are generally not present in graphene films and require specific growth conditions. In contrast, pseudo-magnetic fields can more readily be created in artificial graphene systems either by arranging elements into a pattern that mimics strained "nanobubbles" or by using a specifically engineered coupling pattern with the elements remaining at the nodes of the hexagonal lattice. In addition, at present, artificial lattices with triangular symmetry are being extensively exploited as a platform to explore the physics of topological states.[10–12]

In the present work, we study the band structure of bound electromagnetic modes supported by a plane, hexagonal, perfectly conducting metal-mesh. In contrast to previously considered electromagnetic graphene systems,[6,7,13] our mesh has an exceedingly large ratio of in-plane to out-of-plane dimensions (lattice constant/wire thickness $\approx$200), which is even higher than graphene itself. This system allows for a simple analytical treatment using electric circuit theory, and we demonstrate its benefits in predicting and analysing various graphene-like phenomena. We validate our model via comparison with experimentally measured dispersion curves of the bound electromagnetic waves at microwave frequencies.

The sample was fabricated via conventional lithographic techniques, with the hexagonal pattern being etched into a 19 μm-thick copper layer on a 50 μm thick dielectric substrate. The sample comprises approximately 5000 hexagons of side length $a = 3$ mm and wire width $d = 1$ mm (see Fig. 1).

Electromagnetic modes within the sample are excited and detected using a pair of stripped-end coaxial cables as near-field antennas, each connected to a port of a microwave vector network analyser (VNA). Both antennas are placed with their coaxial axes normal to the sample surface with the metal tips approximately 0.5 mm away from the surface. Source and detection antennas are positioned on opposite sides of the sample to limit direct coupling between them. The detecting probe is raster scanned in 2D across the sample surface with 1 mm step-spacing in both directions. The

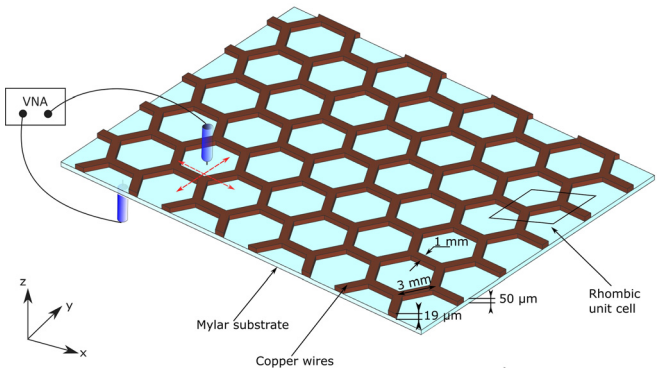

FIG. 1. Schematic representation of the sample studied. It is a copper hexagonal mesh with a thickness of 19 μm on a dielectric substrate with a thickness of 50 μm. The length and width of the wire interconnects are 3 mm and 1 mm, respectively. Source and detection antennas are positioned on opposite sides of the sample and connected to a VNA. Red dashed arrows indicate the scanning directions of the detecting probe.

[a]Electronic mail: y.dautova@exeter.ac.uk

amplitude and relative phase of the local electric field (predominantly the z-component, due to the orientation of the antenna) are measured at each spatial coordinate over a frequency range of 1 to 35 GHz, in 25 MHz steps.[13]

A Fast Fourier Transform (FFT) is then applied to the measured field-data in space to give a 2D map of the modes in momentum space (k_x, k_y) (equi-energy contours). Combining such curves for different frequencies produces the full mode-dispersion.

The measured band structure of the system is plotted in Fig. 2. As can be seen, there are linear Dirac crossings at the corners of the Brillouin zone at K and K' points at a frequency of $f_D = 30$ GHz. The frequency of the Dirac crossings is defined by the parameters of the mesh and is dictated by the resonance frequency of the wires as discussed below.

The structure explored in this study is a simply connected hexagonal mesh formed from metallic wires. It may also be viewed as a triangular lattice with two Y-shaped elements per unit cell (see Fig. 3), with each Y shaped element being equivalent to a carbon atom in graphene itself.

This system supports electric currents propagating in the wires, and so, from electric circuit theory, it is possible to model the expected dispersion of the bound electromagnetic waves. Consider a minimal LC model which is capable of representing the electrodynamics of such a wire-based hexagonal mesh. The primary source of inductance and capacitance is the self-inductance and self-capacitance of the connectors. The currents are obviously flowing in the wires and thereby define the inductance, and since the area of the junctions is small, the capacitance is also defined by the wires.

Let the voltage on each site shown in Fig. 3 be V_X, where X is the site index. For a mode with Bloch wave vector

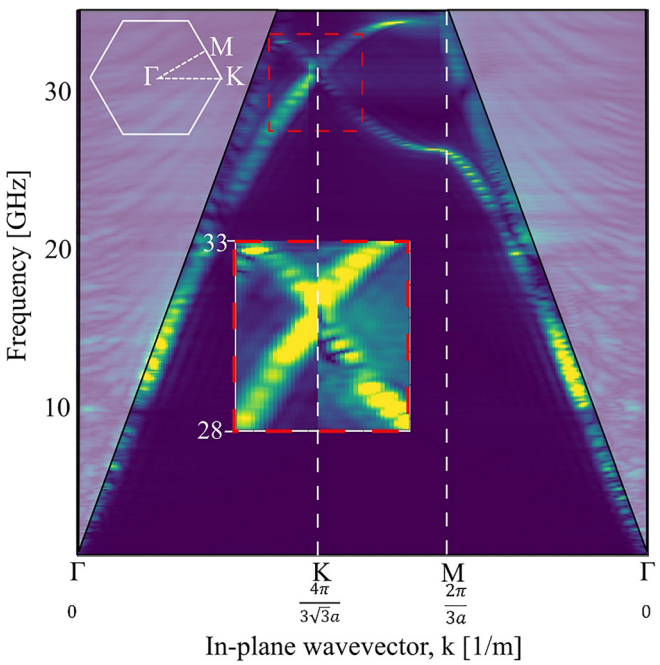

FIG. 2. Dispersion of the electromagnetic bound modes supported by the wire-mesh sample, obtained by FFT of the measured near-field above the surface. Shaded triangular areas indicate the radiative region bound within the light cone. The inset in the red dashed frame is a zoomed view of the area in the vicinity of the Dirac point, normalised to 1.

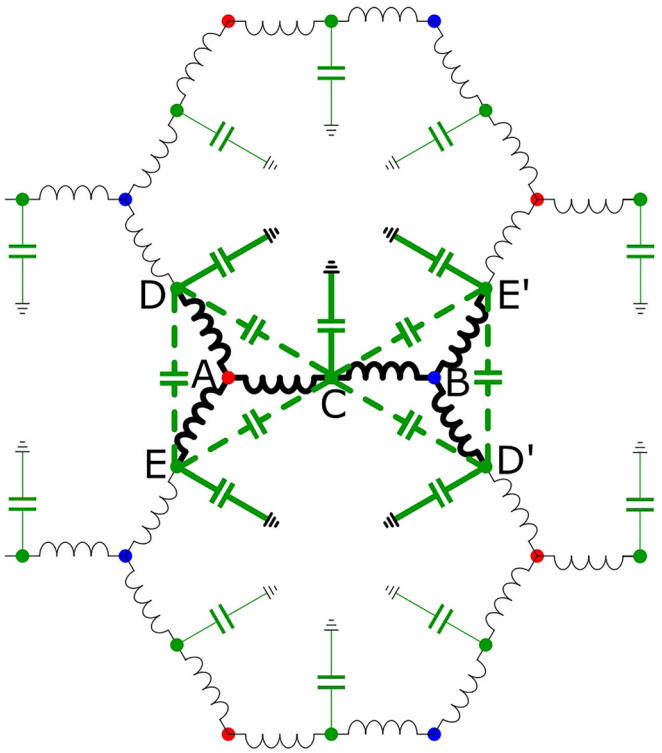

FIG. 3. The circuit model for reproducing the electrodynamics of a wired honeycomb lattice. The unit cell is represented in bold. Capacitors linked by dashed lines represent the mutual capacitance of adjacent wires, which also needs to be taken into account to fully match the observed dispersion.

$\boldsymbol{k} = (k_x, k_y)$, the voltages $V_{D'}$ and $V_{E'}$ can be obtained from the voltages on the sites D and E by applying respective translations as $V_{D'} = V_D \xi_{\boldsymbol{k}} \eta^*_{\boldsymbol{k}}$ and $V_{E'} = V_E \xi_{\boldsymbol{k}} \eta_{\boldsymbol{k}}$. The charges on the nodes C, D, and E are $Q_C = CV_C$, $Q_D = CV_D$, $Q_E = CV_E$, where C is the connector self-capacitance. Note that there is no charge accumulation on the A and B sites. The charges on the capacitors (links) C, D′, and E′ can change due to the current flowing through each link according to the standard capacitor current-voltage relation, $C\frac{dV_X}{dt} = J_{Y\to X} + J_{Z\to X}$, where $X = [C, D', E']$, while Y and Z are the neighboring sites of X. In turn, the currents are related to the relevant voltage drops via Faraday's induction law and the definition of inductance as $-L\frac{dJ_{Y\to X}}{dt} = V_Y - V_X$. Sites A and B participate "passively"—the algebraic sum of currents entering these sites is zero, according to Kirchhoff's law.

To simplify the system of equations, it is convenient to introduce flux variables Φ_X which are defined as $V_X = -d\Phi_X/dt$. These flux variables represent the line integral $\int \boldsymbol{A} \cdot d\boldsymbol{l}$ taken over the line passing through each circuit component, where $\boldsymbol{A}$ is the vector potential. In particular, the flux across an inductor is given by the difference in flux variables between its terminals.

After simple transformations, one can express the currents in terms of the three flux variables. This gives the following equations for the sum of the currents at the points C, D, and E:

$$J_C = \left(4\Phi_C - (1+\xi_{\boldsymbol{k}}\eta^*_{\boldsymbol{k}})\Phi_D - (1+\xi_{\boldsymbol{k}}\eta_{\boldsymbol{k}})\Phi_E\right)/3L,$$
$$J_D = \left(-(1+\xi^*_{\boldsymbol{k}}\eta_{\boldsymbol{k}})\Phi_C - (1+(\eta^2_{\boldsymbol{k}}))\Phi_E + 4\Phi_D\right)/3L,$$
$$J_E = \left(-(1+\xi^*_{\boldsymbol{k}}\eta^*_{\boldsymbol{k}})\Phi_C - (1+(\eta^2_{\boldsymbol{k}})^*)\Phi_D + 4\Phi_E\right)/3L.$$

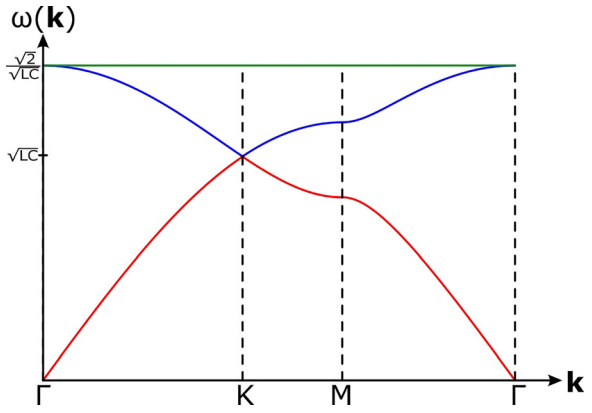

FIG. 4. Dispersion relation obtained from the LC circuit model. The flat mode (green) is an artefact of the minimal LC circuit model.

Here, $\xi_{\boldsymbol{k}} \equiv e^{i3k_x a/2}$, $\eta_{\boldsymbol{k}} \equiv e^{i\sqrt{3}k_y a/2}$, and a is the side of the hexagon cell. On the other hand, $J_X = C\dot{V}_X = -C\ddot{\Phi}_X$. For a mode with frequency ω and assuming time-harmonic waves, we can write $J_X = C\omega^2\Phi_X$. Thus, these three equations define an eigenvalue problem that can be easily solved to yield the dispersion of the modes supported by the mesh. The square of the frequency ω^2 is the eigenvalue to be found, and the flux variables (or potentials) on the sites C, D, and E form an eigenvector for each normal mode.

Let us discuss the mode dispersion that is plotted in Fig. 4. First, one can notice the presence of an unusual flat (zero gradient) branch with the highest frequency (green line). The origin and structure of this mode can be explained as follows: Let us assume that the flux variables Φ_C, Φ_D, $\Phi_{D'}$, Φ_E, and $\Phi_{E'}$ are arranged in such a way that they cancel the flux variables Φ_A and Φ_B (and hence the voltages on all A and B sites). If this is indeed the case, full decoupling should occur as the capacitors are only connected to each other via the A and B sites. In the configuration in which $\Phi_A = \Phi_B = 0$, each capacitor is effectively discharged to ground via the two parallel inductances. In other words, in the analysis of the flat-banded mode, A and B can be replaced with a virtual ground. This is equivalent to an array of decoupled LC-circuits, each of inductance $L/2$ and capacitance C, which gives the degenerate resonant frequency $\sqrt{2}\Omega_0 = \sqrt{2/LC}$.

For the other two modes in Fig. 4, the dispersion is obtained by diagonalizing the eigenvalue equations. This gives

$$\omega^2(\boldsymbol{k}) = \frac{\Omega_0^2}{3}\left(3 \pm \left|2\cos\left(\frac{\sqrt{3}}{2}k_y a\right) + \exp\left(\frac{i3}{2}k_x a\right)\right|\right),$$

where k_x and k_y are the components of the wave vector and a is the side of the hexagon. Unsurprisingly, this reproduces the dispersion law for electrons in graphene found using the framework of the tight-binding model. Similar to real graphene and other artificial graphenes, Dirac crossings at K and K′ points are a result of the lattice symmetry (i.e., two elements per unit cell in the hexagonal array). Near the Γ-point, $\boldsymbol{k} \to 0$, and this solution yields a linear dispersion $\omega(\boldsymbol{k}) = \Omega_0 a|\boldsymbol{k}|/2$. The positions of the Dirac points in the Brillouin zone are determined by requiring that the splitting between the modes vanishes. This condition gives $\boldsymbol{K} = \left(4\pi/3\sqrt{3}a, 0\right)$, $\boldsymbol{K}' = \left(-4\pi/3\sqrt{3}a, 0\right)$ with the frequency $\omega(\boldsymbol{K}) = \Omega_0 = 1/\sqrt{LC}$. By expanding the modulus in the above equation near the K-point (and similarly near the K′-point), one can obtain the mode dispersion in the vicinity of the Dirac points $\omega(\boldsymbol{k}) \approx \Omega_0(1 \pm (|\boldsymbol{k} - \boldsymbol{K}|a)/4)$, where the Dirac velocity is $\Omega_0 a/4$, i.e., one half of the velocity near the Γ-point.

The above presented minimal LC circuit model reproduces both the Dirac crossing at the K-points and qualitatively the shape of the measured dispersion curves. However, a far better comparison between the experimental and analytical dispersion curves is achieved by taking into account the mutual capacitance of the wires C_{mut}. In this more general case, the left-hand side of Eq. (1) is recast in a matrix form as $\widehat{\mathcal{C}}(\boldsymbol{k})\omega^2\Phi$, where $\widehat{\mathcal{C}}(\boldsymbol{k})$ is the capacitance matrix, and $\Phi = (\Phi_C, \Phi_D, \Phi_E)$ is the vector formed by flux variables. The right-hand side is $\widehat{\mathcal{L}}(\boldsymbol{k})\Phi$, where the elements of the matrix $\widehat{\mathcal{L}}$ represent inductances. Hence, the vector formed by the flux variables must satisfy the equation $\omega^2(\boldsymbol{k})\widehat{\mathcal{C}}(\boldsymbol{k})\Phi(\boldsymbol{k}) = \widehat{\mathcal{L}}(\boldsymbol{k})\Phi(\boldsymbol{k})$. Such an equation defines a generalized eigenvalue problem. The dispersion $\omega(\boldsymbol{k})$ is found from the characteristic equation $\det[\widehat{\mathcal{C}}(\boldsymbol{k})\omega^2 - \widehat{\mathcal{L}}(\boldsymbol{k})] = 0$. Matrices $\widehat{\mathcal{C}}(\boldsymbol{k})$ and $\widehat{\boldsymbol{L}}(\boldsymbol{k})$ can be derived from Kirchhoff's laws, or one can analyze the capacitive and inductive contributions to the energy, W_E and W_M. The former contribution is of the form $W_E = V^*\widehat{\mathcal{C}}(\boldsymbol{k})V/2$, where the potentials $V = -\dot{\Phi}$, while the latter is $W_M = \Phi^*\widehat{\mathcal{L}}(\boldsymbol{k})\Phi/2$. Expressing W_E and W_M through the energies stored in each of the circuit capacitors and inductors yields expressions for the capacitance and inductance matrices $\widehat{\mathcal{L}}(\boldsymbol{k})$ and $\widehat{\mathcal{B}}(\boldsymbol{k})$. This eigenvalue problem of the system with the mutual capacitance taken into account is solved numerically. The resulting dispersion of the first two modes is shown in Fig. 5 where it is plotted on top of the experimental data. There is very good agreement between the modeled and measured dispersion curves. To obtain this match, the values of C, C_{mut}, and L used in the model were first estimated from analytical approximations for the capacitance and inductance of a real, square-

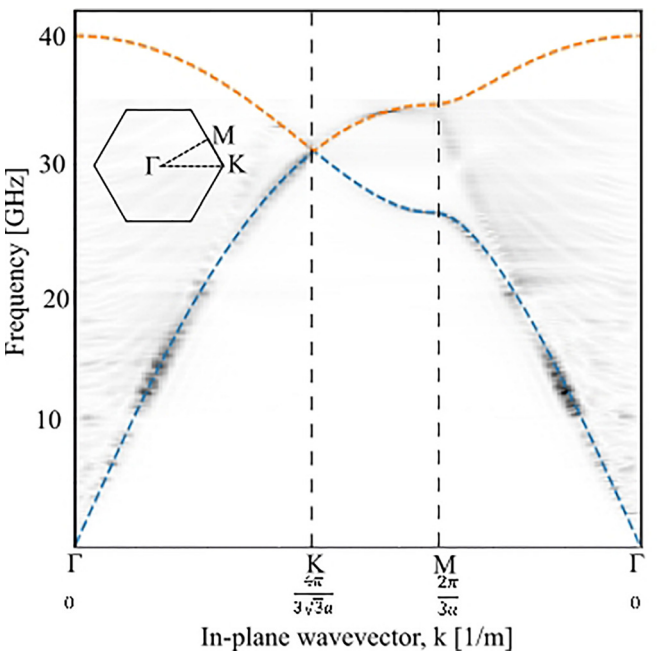

FIG. 5. Mode dispersion obtained through FFT of the experimental data (black and white) and dispersion of the two lowest modes obtained from the LC circuit model (color dashed lines).

shaped wire,[14,15] and then, their values were varied within appropriate bounds until the best match with the experimental data was achieved. The following values were used to obtain the presented dispersion: $C = 0.021$ pF, $C_{\text{mut}} = 0.015$ pF, and $L = 2$ nHn.

In conclusion, we have fabricated a simple metallic hexagonal mesh as a microwave-photonic-analogue to graphene and experimentally measured the bound electromagnetic eigenmodes it supports. We determine the dispersion of these modes and show linear crossings at the K and K′ points of their hexagonal Brillouin zone—mimicking the well-celebrated Dirac cones in real graphene. We propose a simple, analytical LC circuit capable of representing the electrodynamics of the propagating modes. Dispersion curves calculated with this circuit model are shown to fully match the experimental data using realistic values of the inductance and capacitance of the wire mesh. We believe that the results of this work will help in a wider exploration of graphene physics. For instance, in contrast to previously reported microwave graphene systems, the simplicity of the "hexagonal wire-mesh graphene" allows for easy manipulation of the coupling strength between neighboring elements by altering the cross-section of the connectors without changing element positions.

The authors wish to acknowledge the financial support from the Engineering and Physical Sciences Research Council (EPSRC) of the United Kingdom, via the EPSRC Centre for Doctoral Training in Metamaterials (Grant No. EP/L015331/1) and from the Higher Education Funding Council for England (HEFCE). All data created during this research are openly available from the University of Exeter's institutional repository at https://ore.exeter.ac.uk/.

[1]J. D. Joannopoulos, S. G. Johnson, J. N. Winn, and R. D. Meade, *Photonic Crystals: Molding the Flow of Light* (Princeton University Press, 2011).
[2]J.-M. Lourtioz, H. Benisty, V. Berger, J.-M. Gerard, D. Maystre, and A. Tchelnokov, *Photonic Crystals* (Springer, 2005).
[3]E. Yablonovitch, "Inhibited spontaneous emission in solid-state physics and electronics," Phys. Rev. Lett. **58**, 2059 (1987).
[4]S. John, "Strong localization of photons in certain disordered dielectric superlattices," Phys. Rev. Lett. **58**, 2486 (1987).
[5]A. C. Neto, F. Guinea, N. M. Peres, K. S. Novoselov, and A. K. Geim, "The electronic properties of graphene," Rev. Mod. Phys. **81**, 109 (2009).
[6]M. Polini, F. Guinea, M. Lewenstein, H. C. Manoharan, and V. Pellegrini, "Artificial honeycomb lattices for electrons, atoms and photons," Nat. Nanotechnol. **8**, 625–633 (2013).
[7]M. Bellec, U. Kuhl, G. Montambaux, and F. Mortessagne, "Tight-binding couplings in microwave artificial graphene," Phys. Rev. B **88**, 115437 (2013).
[8]T. Uehlinger, G. Jotzu, M. Messer, D. Greif, W. Hofstetter, U. Bissbort, and T. Esslinger, "Artificial graphene with tunable interactions," Phys. Rev. Lett. **111**, 185307 (2013).
[9]N. Levy, S. Burke, K. Meaker, M. Panlasigui, A. Zettl, F. Guinea, A. C. Neto, and M. Crommie, "Strain-induced pseudo–magnetic fields greater than 300 tesla in graphene nanobubbles," Science **329**, 544–547 (2010).
[10]M. C. Rechtsman, J. M. Zeuner, Y. Plotnik, Y. Lumer, D. Podolsky, F. Dreisow, S. Nolte, M. Segev, and A. Szameit, "Photonic floquet topological insulators," Nature **496**, 196–200 (2013).
[11]A. B. Khanikaev, S. H. Mousavi, W.-K. Tse, M. Kargarian, A. H. MacDonald, and G. Shvets, "Photonic topological insulators," Nat. Mater. **12**, 233–239 (2013).
[12]O. P. Sushkov and A. C. Neto, "Topological insulating states in laterally patterned ordinary semiconductors," Phys. Rev. Lett. **110**, 186601 (2013).
[13]Y. N. Dautova, A. V. Shytov, I. R. Hooper, J. R. Sambles, and A. P. Hibbins, "Gapless states in microwave artificial graphene," Appl. Phys. Lett. **110**, 261605 (2017).
[14]Y. Y. Iossel, E. Kochanov, and M. Strunskii, *The Calculation of Electrical Capacitance*, Technical Report (1971).
[15]F. W. Grover, *Inductance Calculations: Working Formulas and Tables* (Instrument Society of America, 1973).